Supporting Information

Özkumur *et al.* 10.1073/pnas.0711421105

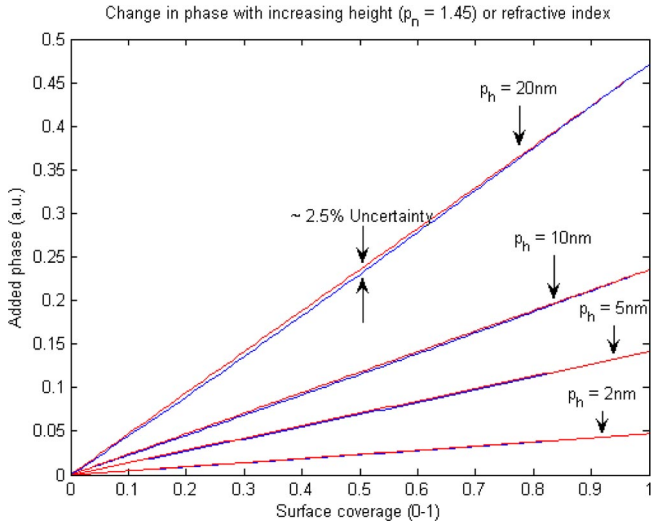

Fig. S1. Linear phase change with increasing surface coverage. The effect of increasing surface coverage on phase is simulated by using both the constant refractive index and constant height approximations. The data are generated by using the transfer matrix method, assuming normal incidence and reflection, for an oxide thickness of 10 μm on silicon and an extra-thin layer representing the biomolecular accumulation. For the constant index simulations, the height of the biomolecular layer was linearly increased from 0 to p_h, the physical height of the monolayer, as the surface coverage was assumed to increase from 0 to 1 (no accumulation to complete coverage), and the refractive index of the layer was assumed to be 1.45. For the constant-height simulations, the refractive index of the layer was linearly increased from 1.33 (water) to 1.45 (protein) as the surface coverage was increased from 0 to 1, and the height of the layer was taken as p_h. Then these two datasets were processed by the same algorithm, which assumes reflections present only from oxide and silicon, and finds the added phase as a result of added index or height. The results are shown in the above plots. Both the constant index and constant height approximations give nearly identical results and increase almost linearly for layer thicknesses that are much smaller than the wavelength. The constant-height approximation starts to give nonlinear results after the layer thicknesses are $>$20 nm, which is quite unlikely for protein microarrays. The difference between constant index and constant-height approximations was calculated as 5% error for a small surface coverage and decreasing to 0 as the layer approaches a uniform coverage (in which case, the two models merge). As these results indicate, the phase retardation is independent of conformation of the biomolecules of interest; a conformational height increase would decrease the surface coverage, and so decrease the refractive index while increasing the height of the layer. As the both are linearly related, the phase is effected minimally from such conformational changes that are $<$20 nm. Finally, as it is also pointed by several researchers, presetting the biomolecular layer refractive index to 1.45 and measuring the height does not reflect the real dimensions of layer height. But the surface-adsorbed mass density measured this way is still correct (1, 2).

1. Prime KL, Whitesides GM (1991) Self-assembled organic monolayers: Model systems for studying adsorption of proteins on surfaces. *Science* 252:1164–1167
2. Voros J (2004) The density and refractive index of adsorbing protein layers. *Biophys J* 87:553–561

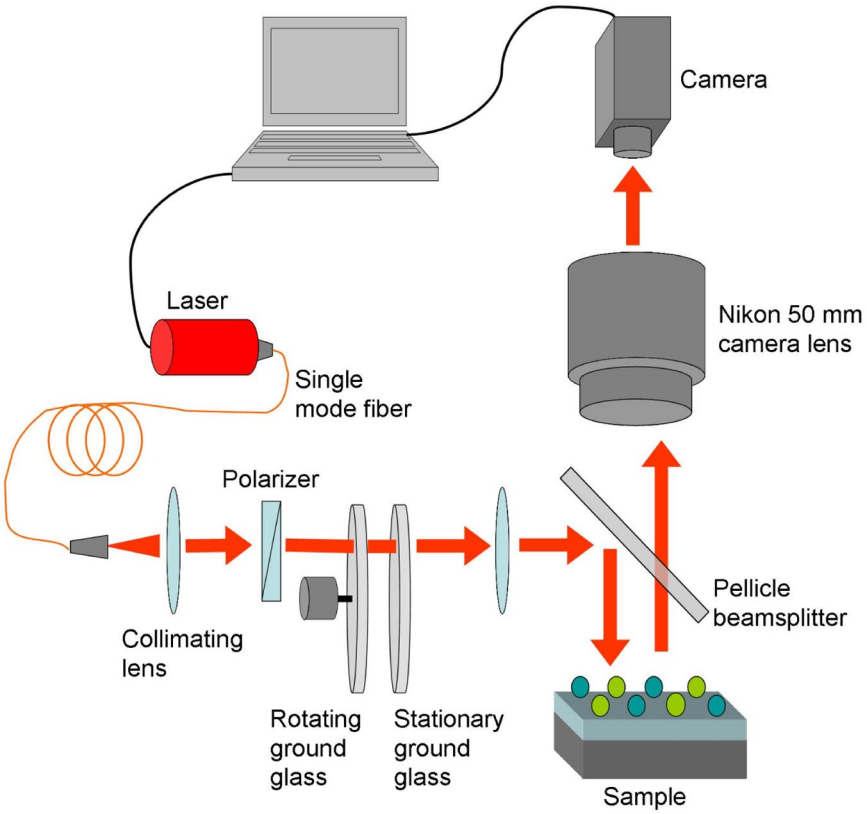

Fig. S2. Experimental setup. The laser was first collimated with a single lens and polarized by using a polarizing beam splitter. The beam is then passed through two ground-glass disks, where one of them is rotating. The diffused light is collected by a second lens to condense the illumination on the sample. The sample is a silicon chip with $\approx$10 μm of oxide on it, which is thick enough to have a whole period of the sinusoidal signal in the tuning range. Reflected light is imaged on a CCD camera using a Nikon 50-mm camera lens.

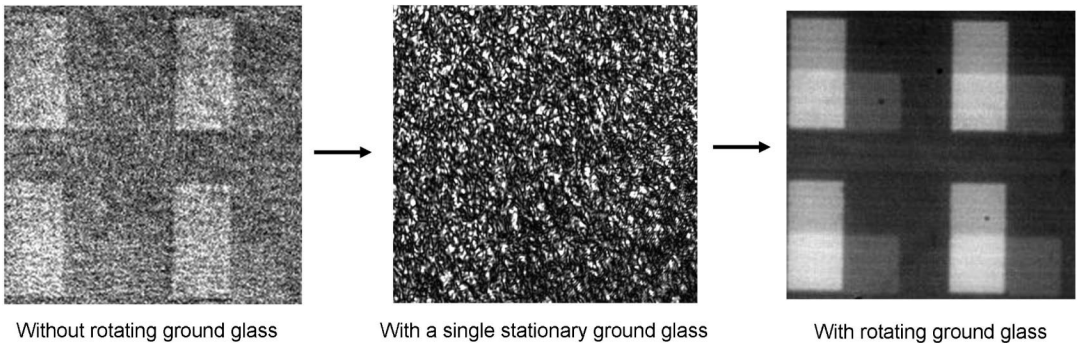

Fig. S3. Improvement with rotating ground glass. Effects of coherent illumination on imaging has been discussed before, and several methods have been proposed to randomize the spatial coherency of the laser such as the use of multiple wave illumination (1), liquid crystals (2), ultrasound light modulators (3), and moving diffusers (4, 5). In our system, we chose to pass the illumination beam through two ground-glass disks, where at least one is rotating, reducing the spatial coherence dramatically, thus eliminating the related artifacts in the image.

1. Upatnieks J, Lewis RW (1973) Noise suppression in coherent imaging. *Appl Opt* 12:2161–2166.
2. Scudieri F, Bertolotti M, Bartolino R (1974) Light scattered by a liquid crystal: A new quasi-thermal source. *Appl Opt* 13:181–185.
3. Imai Y, Ohtsuka Y (1980) Optical coherence modulation by ultrasonic waves. 1: Dependence of partial coherence on ultrasonic parameters. *Appl Opt* 19:542–547.
4. Considine PS (1966) Effects of coherence on imaging systems. *J Opt Soc Am* 56:1001–1009.
5. Hard R, Zeh R, Allen RD (1977) Phase-randomized laser illumination for microscopy. *J Cell Sci* 23:335–343.

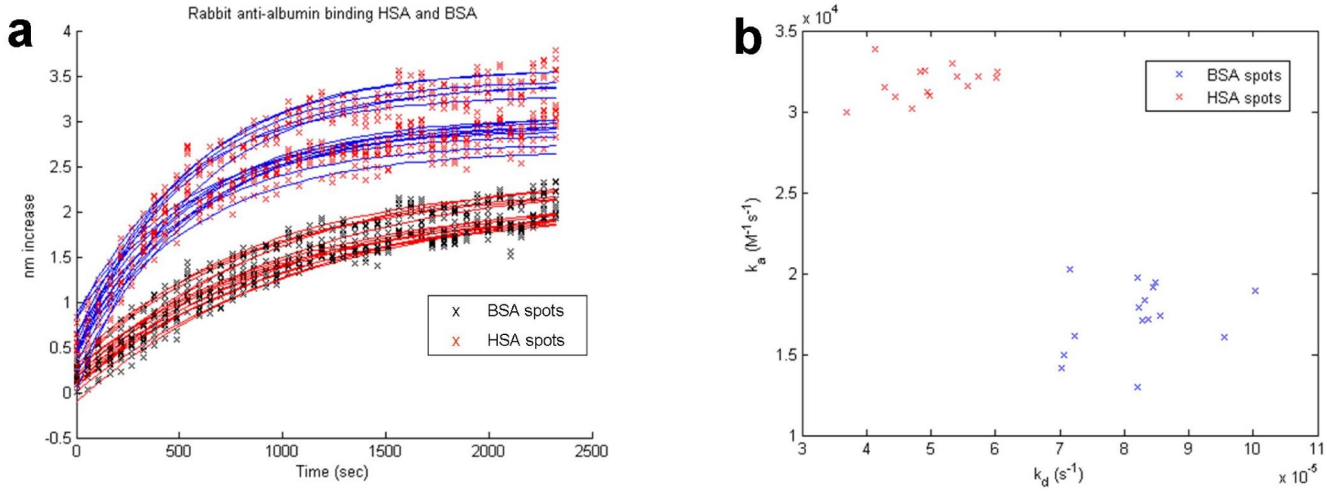

Fig. S4. Calculation of reaction rates for HSA and BSA. For both HSA and BSA, binding kinetics were assumed to obey the relation:

$$X + Y \underset{k_a}{\overset{k_d}{\rightleftharpoons}} \mathrm{XY}, \qquad [1]$$

where X is the amount of free antibody, Y is the amount of bound antigen, XY is the complex, and k_a and k_d are the "on" and "off" rates, respectively. Then the equilibrium constant for association would be $K_A = k_a/k_d$. The amount of XY complex during association is given by:

$$[XY] = [Y]_0(1 - e^{-k_{\mathrm{obs}}t}) + \text{constant}, \qquad [2]$$

where $k_{\mathrm{obs}} = k_a\,[X]_0 + k_d$. During dissocciation:

$$[XY] = [XY]_0 e^{-k_d t}. \qquad [3]$$

(*a*) We used least-squares method to solve for k_d and k_{obs}, by fitting exponential curves to the recorded data. Knowing $[X]_0$, k_a was calculated from the above relationship. (*b*) Even though there exists a clear difference between the distributions of HSA and BSA in the k_a and k_d space, they both respond to anti-HSA because they have a significant sequence identity (as determined by NCBI's protein BLAST program).

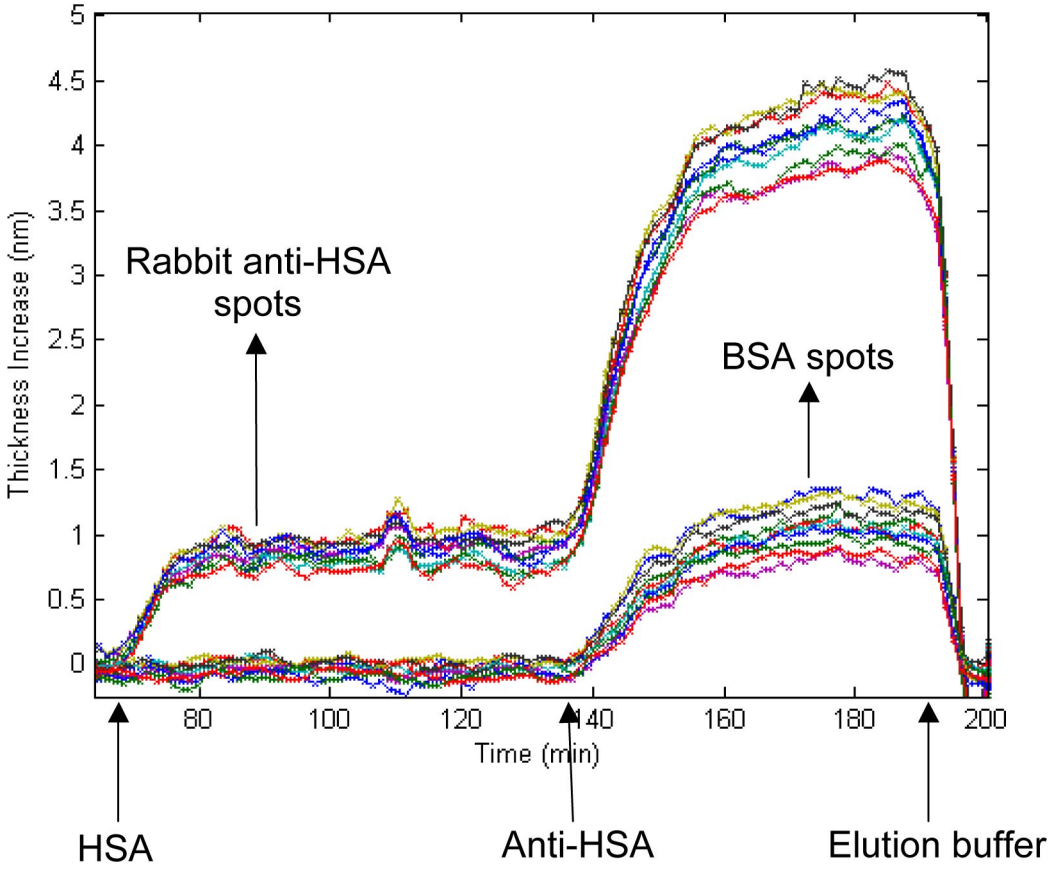

Fig. S5. Simultaneous detection of human serum albumin antigens and antibodies. To demonstrate the simultaneous detection of antigens and antibodies, a substrate was prepared with 10 spots of rabbit anti-HSA and 10 spots of BSA. Both proteins were biotinylated and spotted on a streptavidin surface at ≈1 mg/ml concentrations in 1× PBS containing 2.5% glycerol and 0.1% Tween-20. The chip was left to incubate overnight, washed, and placed in the flow chamber. After blocking the surface with synthetic blocking buffer (cat. no. 4520L; Kim-En-Tec Diagnostics) and washing with PBST, the sample was first incubated with HSA (10 μg/ml in PBST) and then with rabbit anti-HSA (10 μg/ml in PBST). The instances when these analytes were introduced are indicated in the figure. In the first incubation, the HSA proteins were captured by the spotted anti-HSA antibodies. In the second incubation step, the binding of immobilized antibodies in the solution to the previously immobilized antigens was detected. In this step, binding of anti-HSA to spotted BSA was also detected as a result of the cross-reactivity between the two molecules. Finally, the antigen–antibody bonds were defunctionalized with the elution buffer, and the bound biomolecules were released.

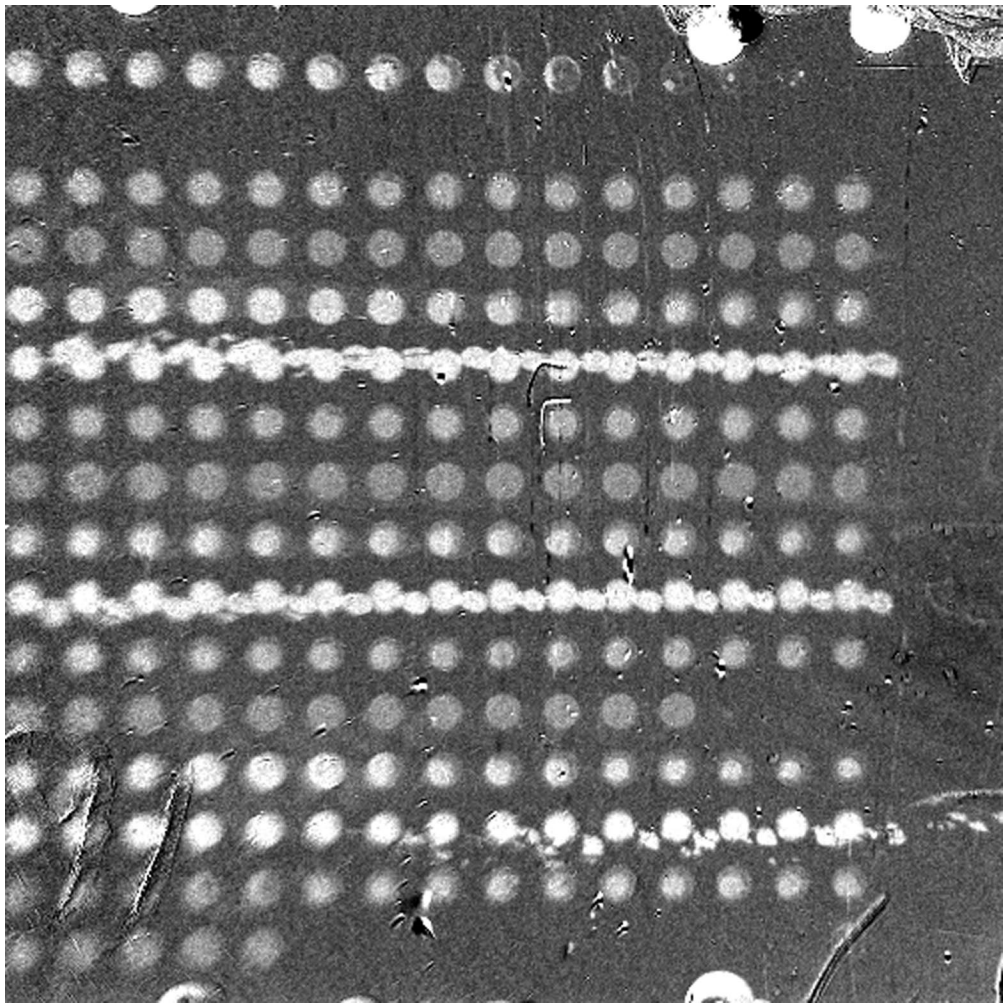

Movie S1. Dynamic imaging of multiple binding events. The binding events were monitored in real time for an array of 208 spots. Each row of spots contains the same probe biomolecule. Because all the frames are referenced to an initial image, spots are not visible without binding. By the introduction of anti-mouse IgG, protein G spots light up as a result of binding. Rabbit IgG spots also become visible at this stage as a result of cross-reactivity. Then the rabbit IgG spots became more visible when anti-rabbit IgG was introduced. The HSA and BSA spots lit up when the sample was incubated with anti-HSA. Finally, with the acidification, the antibodies were released from their antigens. Time lapse of the movie is ≈ 270 min. The floating particles create the major noise source in the images, but they are easily filtered from the dynamic curves presented in Fig. 3 because they create very distinct spikes in the height data. The deformations on the rabbit IgG spots are caused by the smearing of the spotted probes during washing.

Movie S1 (MOV)